

## Various Approaches to Cosmological Gravitational Lensing in Inhomogeneous Models

Kenji TOMITA<sup>1,\*</sup>), Premana PREMADI<sup>2,\*\*</sup>) and Takahiro T. NAKAMURA<sup>3,\*\*\*</sup>)

<sup>1</sup> *Yukawa Institute for Theoretical Physics, Kyoto University, Kyoto 606-8502, Japan*

<sup>2</sup> *Astronomical Institute, Tohoku University, Sendai 980-8578, Japan*

<sup>3</sup> *Department of Physics, The University of Tokyo, Tokyo 113-0033, Japan*

(Received February 10, 1999 )

Gravitational lensing of distant objects caused by gravitational tidal forces from inhomogeneities in the universe is weak in most cases, but it is noticed that it gives a great deal of information about the universe, especially regarding the distribution of dark matter. The statistical values of optical quantities such as convergence, amplification and shear have been derived by many people using various approaches, which include the linear perturbational treatment in the weak limit and the nonlinear treatment considering small-scale matter distribution.

In this review paper we compare the following three main approaches: (a) the approach in the multi-lens-plane theory; (b) the approach due to the direct integration method; and (c) the perturbational approach.

In the former two approaches inhomogeneous matter distributions are produced in the CDM model using  $N$ -body simulations (the  $P^3M$  code and the tree-code, respectively). In (c) the power spectrum corresponding to the CDM model is used for the large-scale matter distribution.

### §1. Introduction

The propagation of light from distant objects like galaxies and QSOs is deflected by the gravitational tidal forces caused by inhomogeneous matter distribution between the objects and us. The so-called lens effect creates conspicuous images such as multiple QSOs and arcs in clusters of galaxies, owing to special positional relations among sources, lens objects and the observer, but in most cases it causes small deformations and amplification of optical images, which result from the superposition of deflections from many lens objects on cosmological scales. This so-called weak lensing gives us valuable information on the structure and evolution of the universe, especially regarding the distribution of dark matter, not only on large scales, but also on small scales around galaxies.

The statistical behavior of optical quantities such as convergence, amplification and shear due to weak lensing has been studied by many people since the pioneering papers by Gunn,<sup>1)</sup> Weinberg<sup>2)</sup> and Blandford and Jaroszyński.<sup>4)</sup> For the derivations of these quantities there have been various approaches which consist of the multi-lens-plane method, direct integration methods solving the null-geodesic

---

\*) E-mail address: tomita@yukawa.kyoto-u.ac.jp

\*\*) E-mail address: premadi@astr.tohoku.ac.jp

\*\*\*) E-mail address: nakamura@utaphp2.phys.s.u-tokyo.ac.jp

equation, optical scalar equations and the equation of geodesic deviation, and perturbative methods.

### 1.1. *Multi-lens-plane method*

This is one of the various methods numerically simulating light propagation in inhomogeneous model universes, which were derived and developed by Blandford and Narayan,<sup>6)</sup> Schneider and Weiss,<sup>7) - 8)</sup> Jaroszyński et al.,<sup>9)</sup> Jaroszyński.<sup>10) - 11)</sup> In this method we first build a finite number of planes normal to light rays between an observer and a source, and the three-dimensional distribution of galaxies and dark matter as lens objects is replaced by their two-dimensional distribution in the planes onto which the matter in each interval is projected. The deflection of light rays resulting from each lens plane is calculated using geometrical optics, and the statistical averages of optical quantities for many-ray bundles are derived.<sup>5)</sup>

To use this method we must produce the inhomogeneous distribution of lens objects in each lens plane. In early works (Schneider and Weiss,<sup>8)</sup> Paczyński and Wambsganss,<sup>12)</sup> Lee and Paczyński.<sup>13)</sup>) the random distribution of lens objects with an equal mass was assumed, and so the realistic large-scale structure of the matter distribution was neglected. Jaroszyński et al.<sup>9)</sup> constructed an inhomogeneous model using an  $N$ -body simulation (the PM code), but in this model large-scale structure was considered, while small-scale structure corresponding to galaxies was neglected. Jaroszyński<sup>10) - 11)</sup> developed other numerical models of matter distribution using the Zeldovich approximation, located galaxies (as lens objects) corresponding to the matter density, and assumed for them the mass spectrum due to the Schechter luminosity function and their morphological types randomly.

Wambsganss et al.<sup>14) - 15)</sup> generated models for the evolution of large-scale structures by  $N$ -body simulation in the CDM models, investigated their influence on light propagation and statistical results such as the frequency and separation angles of multiple QSOs and the image deformation of high-redshift objects. In their works, galaxies as lens objects were not taken into account.

Recently Premadi et al.<sup>16)</sup> have improved the work of Jaroszyński et al. by adopting an  $N$ -body simulation (P<sup>3</sup>M code) and considering the spatial distribution of galaxies with the mass spectrum and morphological types (due to the morphological type-density relation). They adopted Jaroszyński's assumption that the main lens objects are galaxies and the background matter outside galaxies has smooth distribution with radii  $\approx 1h^{-1}$  Mpc. In §2 the recent result of studies by Premadi et al.<sup>16)</sup> is given.

### 1.2. *Direct integration methods*

There are three types of direct integration methods in which the optical scalar equation (derived by Sachs<sup>17)</sup>), the equation of geodesic deviation and the null-geodesic equation are solved. Kantowski's approach belongs to the first type. He derived the averaged optical scalar equation and solved it in an inhomogeneous model universe with swiss cheese structure.<sup>18)</sup> Dyer and Roeder<sup>19)</sup> studied the behavior of the amplification applying this approach to the case of a nonzero cosmological constant. Recently, Kantowski et al.<sup>20)</sup> have analyzed the lens effect in the observed redshift-magnitude relation for type Ia supernovae. Watanabe and Tomita<sup>21)</sup> studied the behavior of shear in the ray bundles in various models in which the random

distribution of particles simulating galaxies and clusters of galaxies was assumed for simplicity. As an example of the second type of direct integration method (treating the equation of geodesic deviation) we cite a recent work of Holz and Wald,<sup>22)</sup> who studied the behavior of amplification in an inhomogeneous model with a swiss cheese-like structure. In their case not all systems consisting of a central galaxy and the surrounding empty region have the compensated mass distribution, in contrast to Kantowski's swiss cheese system. They derived the probability distribution of amplification, which was found to be non-Gaussian in accord with Dyer-Oattes<sup>23)</sup> and examined the significance of the amplification on the observation of type Ia supernovae (Holz<sup>24)</sup>). A drawback of this approach may be that it treats only ray bundles with infinitesimal separation angles.

The third type of direct integration method is described in the works of Tomita and Watanabe.<sup>25) - 26)</sup> They treated the multiple deflection of light rays directly by solving the null-geodesic equation and studied the statistical averages of image deformation in inhomogeneous universe models. The evolution of models was derived under the periodic condition using Aarseth's individual particle method for  $N$ -body simulations, in which particles are regarded as galaxies or clusters of galaxies with the initial power spectrum  $n = 0$ . The particles (with the same mass and particle number  $N = 1331$ ) are placed and move in a periodic box with comoving length  $\approx 50$  Mpc, and light rays also propagate in the box under gravitational forces from particles in the box. In Tomita and Watanabe,<sup>25)</sup> the influence of lensing on the CMB anisotropy was analysed and a negative result was obtained, contrary to expectations (Kashlinsky,<sup>27)</sup> Tomita,<sup>28) - 29)</sup> Sasaki.<sup>30)</sup> In the latter paper,<sup>26)</sup> examples of strong image deformations and their statistics were studied. Using the same approach, Tomita<sup>31) - 33)</sup> has recently studied the statistical behavior of optical scalars in more realistic inhomogeneous models with the CDM spectrum ( $n = 1$ ). All particles are assumed to have the same galactic mass, while their radii depend on the model used. In the first two of these papers,<sup>31) - 32)</sup> the lens effect was analyzed in flat and open models, respectively, and in the third paper,<sup>33)</sup> the distribution of angular diameter distances in these models was derived.

As for the number density of main lens objects, there is an important difference between the work of Premadi and that of Tomita. In the former, adopting Jaroszyński's assumption mentioned above, the density of main lens objects (galaxies) is found to be  $\Omega_g \approx 0.02$ . In Tomita's works, on the other hand, the density ( $\Omega_L$ ) of main lens objects (called *compact lens objects*) is  $\Omega_L = 0.2$  for three models with  $\Omega_0 = 1$  and  $0.2$  and  $\Omega_L = 0.4$  for a model with  $\Omega_0 = 0.4$ , which are much larger than  $\Omega_g$ . This difference between these two works comes from the different estimation for the role of non-galactic clouds as lenses. At present it is not clear whether Jaroszyński's assumption is realistic or not, and so the matter outside galaxies may not be so smooth and may behave as discrete clouds with radii  $r_{cl} \approx 100$  kpc, consisting of dark matter and the baryon fluid. In these clouds a baryon fluid has experienced no dissipated collapse and has less central concentration than in galaxies, but as weak lens objects they may play a role similar to galaxies.

An outline of Tomita's recent works is given in §3, and the results of additional analyses are also given in the case (satisfying Jaroszyński's assumption) that the

density of lens objects is  $\Omega_L = \Omega_g$  and the remaining objects are assumed to be smoother, by constraining their radii so as to be  $500h^{-1}\text{kpc}$ . By comparing the two results in the case of  $\Omega_L = 0.2$  and the case of  $\Omega_L = \Omega_g$ , we find how lensing on the small scale is dominated by non-galactic lens objects, if they exist.

### 1.3. *Perturbative methods*

The method for solving optical scalar equations perturbatively with respect to a small perturbed expansion and shear has been introduced by Gunn<sup>2)</sup> and developed by Babul and Lee<sup>34)</sup> and Blandford et al.<sup>35)</sup>. Gravitational influences from large-scale structures are involved in the terms giving the Ricci and Weyl focusing, through the density power spectrum or the numerically simulated matter distribution. The angular correlation functions of optical scalars were derived in connection with the two-point density correlation function, and higher correlations also were studied by Villumsen,<sup>36)</sup> Bernardeau<sup>37)</sup> and Nakamura.<sup>38)</sup>

The perturbative formulation for the image deformations has been derived independently from the null-geodesic equation (Linder,<sup>39)</sup> Martinez et al.,<sup>40)</sup> Martinez and Sanz<sup>41)</sup>). This approach also has been applied to studies concerning weak image deformation of high-redshift objects and the smoothing of the CMB anisotropy (Cayon et al.,<sup>42)</sup> Seljak<sup>43)</sup> and Jain and Seljak<sup>44)</sup>). In §4, a recent result obtained using the power spectrum approach by Nakamura is given.

## §2. Lensing in the multi-lens-plane method

### 2.1. *Methodology*

The inhomogeneities that perturb a light bundle as it travels from a source to an observer are of sizes much smaller than the distance that the light traverses. This has motivated a number of authors to use the multi-plane gravitational lensing approach to study how light propagates in inhomogeneous universes (e.g. Schneider and Weiss,<sup>7)-8)</sup> Jaroszyński et al.,<sup>9)</sup> Jaroszyński,<sup>10)-11)</sup> Wambsganss, Cen and Ostriker<sup>15)</sup>). In this approach one first idealizes the inhomogeneities as being distributed on a series of thin lens planes which are arranged perpendicular to the line of sight. Then one assumes that lensing only occurs in each of those planes. This way one can analyze the lensing properties of each plane separately and let the light beam carry the lensing effect of each plane while propagating from one plane to the next. For this paper to be self-contained we give a brief review of multi-plane lensing theory, following closely the description and notation of Schneider et al.<sup>5)</sup>

### 2.2. *Multi-plane gravitational lensing*

Consider  $N$  lens planes located at redshifts  $z_i$ , with  $i = 1, N$ , and ordered such that  $z_i < z_j$  for  $i < j$ . Figure 1 displays an example with  $N = 2$ . All angles are exaggerated for clarity. Each lens plane is characterized by its respective surface mass density  $\sigma_i(\boldsymbol{\xi}_i)$ , where  $\boldsymbol{\xi}_i$  is the impact vector of the ray in the  $i$ -th lens plane. Let  $\hat{\alpha}_i(\boldsymbol{\xi}_i)$  denote the deflection angle the light ray experiences in the  $i$ -th plane at

a position  $\boldsymbol{\xi}_i$ . From this geometry, we can derive the *lens equation*,

$$\boldsymbol{\eta} = \frac{D_S}{D_1} \boldsymbol{\xi}_1 - \sum_{i=1}^N D_{iS} \hat{\boldsymbol{\alpha}}_i(\boldsymbol{\xi}_i), \quad (2.1)$$

where  $\boldsymbol{\eta}$  is the source position vector (in the source plane),  $\boldsymbol{\xi}_i$  is the impact vector in the  $i$ -th plane,  $D_j$  is the angular diameter distance between the  $j$ -th plane and the observer, and  $D_{ij}$  is the angular diameter distance between the  $i$ -th and  $j$ -th planes, with  $S \equiv N + 1$  identifying the source plane. Knowing the impact vector  $\boldsymbol{\xi}_1$  in the image plane, the impact vector in subsequent planes can be obtained recursively using

$$\boldsymbol{\xi}_j = \frac{D_j}{D_1} \boldsymbol{\xi}_1 - \sum_{i=1}^{j-1} D_{ij} \hat{\boldsymbol{\alpha}}_i(\boldsymbol{\xi}_i). \quad (2.2)$$

The deflection angle is related to the surface density by

$$\hat{\boldsymbol{\alpha}}_i(\boldsymbol{\xi}) = \frac{4G}{c^2} \iint \sigma_i(\boldsymbol{\xi}') \frac{\boldsymbol{\xi}_i - \boldsymbol{\xi}'}{|\boldsymbol{\xi}_i - \boldsymbol{\xi}'|^2} d^2 \xi', \quad (2.3)$$

where  $G$  is the gravitational constant,  $c$  is the speed of light, and the integral extends over the lens plane. We can rewrite this expression conveniently as

$$\hat{\boldsymbol{\alpha}}_i(\boldsymbol{\xi}_i) = \nabla \hat{\psi}_i(\boldsymbol{\xi}_i), \quad (2.4)$$

$$\hat{\psi}_i(\boldsymbol{\xi}_i) = \frac{4G}{c^2} \iint \sigma_i(\boldsymbol{\xi}') \ln |\boldsymbol{\xi}_i - \boldsymbol{\xi}'| d^2 \xi'. \quad (2.5)$$

It is useful to rewrite these equations in a dimensionless form. Define for each lens plane a critical surface density as

$$\sigma_{i,\text{cr}} = \frac{c^2 D_S}{4\pi G D_i D_{iS}}, \quad (2.6)$$

and introduce the following dimensionless quantities :

$$\mathbf{x}_i = \frac{\boldsymbol{\xi}_i}{D_i}, \quad 1 \leq i \leq N + 1; \quad (2.7)$$

$$\kappa_i(\mathbf{x}_i) = \frac{\sigma_i}{\sigma_{i,\text{cr}}}, \quad 1 \leq i \leq N. \quad (2.8)$$

Equations (2.2), (2.4) and (2.5) reduce to

$$\mathbf{x}_j = \mathbf{x}_1 - \sum_{i=1}^{j-1} \beta_{ij} \boldsymbol{\alpha}_i(\mathbf{x}_i), \quad (2.9)$$

$$\boldsymbol{\alpha}_i(\mathbf{x}_i) = \nabla \psi_i(\mathbf{x}_i), \quad (2.10)$$

$$\psi_i(\mathbf{x}_i) = \frac{1}{\pi} \iint \kappa_i(\mathbf{x}') \ln |\mathbf{x}_i - \mathbf{x}'| d^2 x', \quad (2.11)$$

where

$$\beta_{ij} = \frac{D_{ij} D_S}{D_j D_{iS}}, \quad (2.12)$$

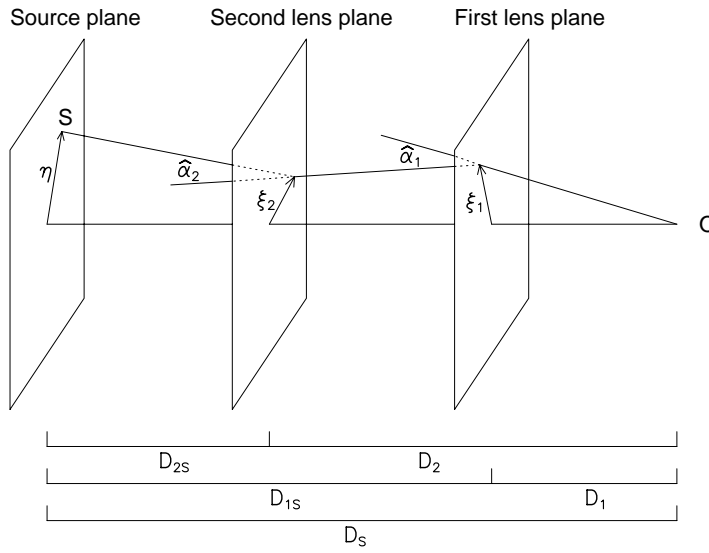


Fig. 1. Multi-lens-planes.

and the gradient is now taken relative to  $\mathbf{x}_i$ . We can invert equation (2.11) and obtain

$$\nabla^2 \psi_i = 2\kappa_i. \quad (2.13)$$

To compute the scaled position  $\mathbf{y} \equiv \mathbf{x}_S$  of the source in the source plane, we simply set  $j = N + 1$ . Equation (2.12) gives  $\beta_{iS} = 1$ , and Eq. (2.9) becomes

$$\mathbf{y} \equiv \mathbf{x}_{N+1} = \mathbf{x}_1 - \sum_{i=1}^N \boldsymbol{\alpha}_i(\mathbf{x}_i). \quad (2.14)$$

This ray-tracing equation is a mapping from the image plane ( $i = 1$ ) onto the source plane ( $i = N + 1$ ).

The effect of each lens plane on the evolution of the beam is described by the Jacobian matrix

$$\mathbf{A}_i(\mathbf{x}_i) = \begin{pmatrix} 1 - \psi_{i,11} & -\psi_{i,12} \\ -\psi_{i,21} & 1 - \psi_{i,22} \end{pmatrix}, \quad (2.15)$$

where the commas denote differentiation with respect to the components of  $\mathbf{x}_i$ . Since  $\psi_{i,12} = \psi_{i,21}$ , and Eq. (2.13) gives  $\psi_{i,11} + \psi_{i,22} = 2\kappa_i$ , we can rewrite Eq. (2.15) as

$$\mathbf{A}_i = \begin{pmatrix} 1 - \kappa_i - S_{11} & -S_{12} \\ -S_{12} & 1 - \kappa_i + S_{11} \end{pmatrix}, \quad (2.16)$$

where

$$S_{11} = \frac{1}{2}(\psi_{i,11} - \psi_{i,22}), \quad (2.17)$$

$$S_{12} = \psi_{i,12} = \psi_{i,21}. \quad (2.18)$$

We now define

$$S_i = (S_{11}^2 + S_{12}^2)^{1/2}. \quad (2.19)$$

The determinant and trace of  $\mathbf{A}_i$  can be expressed entirely in terms of  $\kappa_i$  and  $S_i$ , as follows:

$$\det \mathbf{A}_i = (1 - \kappa_i)^2 - S_i^2, \quad (2.20)$$

$$\text{tr} \mathbf{A}_i = 2(1 - \kappa_i). \quad (2.21)$$

The quantities  $\mu_i \equiv 1/(\det \mathbf{A}_i)$ ,  $1 - \kappa_i$ , and  $S_i$  are called the *magnification*, *convergence* (or Ricci focusing), and *shear*, respectively.

To compute the cumulative effect of all the lens planes, we consider the Jacobian matrix of the mapping given by Eq. (2.14),

$$\mathbf{B}(\mathbf{x}) = \frac{\partial \mathbf{y}}{\partial \mathbf{x}_1} = \mathbf{I} - \sum_{i=1}^N \frac{\partial \boldsymbol{\alpha}_i}{\partial \mathbf{x}_1} = \mathbf{I} - \sum_{i=1}^N \mathbf{U}_i \mathbf{B}_i, \quad (2.22)$$

where  $\mathbf{I}$  is the  $2 \times 2$  identity matrix, and  $\mathbf{U}_i$  and  $\mathbf{B}_i$  are defined by

$$\mathbf{U}_i = \frac{\partial \boldsymbol{\alpha}_i}{\partial \mathbf{x}_i}, \quad (2.23)$$

$$\mathbf{B}_i = \frac{\partial \mathbf{x}_i}{\partial \mathbf{x}_1}. \quad (2.24)$$

After substituting Eq. (2.10) into Eq. (2.23), we obtain

$$\mathbf{U}_i = \mathbf{I} - \mathbf{A}_i = \begin{pmatrix} \psi_{i,11} & \psi_{i,12} \\ \psi_{i,21} & \psi_{i,22} \end{pmatrix}, \quad (2.25)$$

where  $\mathbf{A}_i$  is given by Eq. (2.15). Hence,  $\mathbf{U}_i$  describes the effect the  $i$ -th plane would have on the beam if all the other planes were absent, and Eq. (2.22) simply combines

the effect of all the planes. To compute the matrices  $\mathbf{B}_i$ , we differentiate Eq. (2.9) and get

$$\mathbf{B}_j = \mathbf{I} - \sum_{i=1}^{j-1} \beta_{ij} \mathbf{U}_i \mathbf{B}_i. \quad (2.26)$$

Since  $\mathbf{B}_1 = \mathbf{I}$ , we can use Eq. (2.26) to compute all matrices  $\mathbf{B}_i$  by recurrence.

### 2.3. The numerical algorithm

We use the P<sup>3</sup>M algorithm (Hockney and Eastwood<sup>45</sup>) for the  $N$ -body simulations of the large scale structure (LSS) of the universe. The calculations evolve a system of gravitationally interacting particles in a cubic volume with triply periodic boundary conditions, comoving with the Hubble flow. The forces on the particles are computed by solving the Poisson equation on a cubic grid using a Fast Fourier Transform method.

#### 2.3.1. Building the lens planes

To implement the multi-plane lens method, we divide the space between the source and the observer into a chain of cubic boxes of equal comoving size,  $L_{\text{box}}$ . We first need to determine the redshifts of the interfaces between these cubic boxes. Let us assume that the photons that reach the observer at present entered a particular box at time  $t'$  and redshift  $z'$  and exited that box at time  $t$  and redshift  $z$ . The redshifts  $z'$  and  $z$  are related by (Premadi et al.<sup>16</sup>)

$$L_{\text{box}} = \int_{t'}^t [1 + z(t)] c dt. \quad (2.27)$$

Using this equation, with the appropriate relation for  $z(t)$ , we can find the redshifts of the interfaces. The front side of the box closest to the the observer is, by definition, at  $z = 0$ . Plugging this value into Eq. (2.27) gives us the redshift  $z'$  of the back side of the box, which is also the redshift  $z$  of the front side of the next box. Then, by using Eq. (2.27) recursively, we can compute the redshifts of all the interfaces.

As the structures inside the box might evolve while the light beam travels across it, we decide the plane onto which we project the mass distribution to be at redshift where the density contrast is equal to the time-averaged density contrast of the box.

#### 2.3.2. The galaxy distribution

We consider the LSS at present ( $z = 0$ ) resulting from the P<sup>3</sup>M simulations, and we design an empirical Monte-Carlo method for locating galaxies in the computational volume, based on the constraints that (1) galaxies should be predominantly located in the densest regions, and (2) the resulting distribution of galaxies should resemble the observed distribution on the sky. Our method is the following. We divide the present computational volume into  $128^3$  cubic cells of size  $1 \text{ Mpc}^3$ , and compute the matter density  $\rho$  at the center of each cell using the same mass assignment scheme as in the P<sup>3</sup>M code. We then choose a particular density threshold  $\rho_t$ . We locate  $N$  galaxies in each cell, where  $N$  is given by

$$N = \text{int} \left( \frac{\rho}{\rho_t} \right). \quad (2.28)$$



The actual location of each galaxy is chosen to be the center of the cell, plus a random offset that is of the order of the cell size. This eliminates any spurious effect introduced by the use of a grid. We then experiment with various values of the density threshold  $\rho_t$  until the total number of galaxies comes out to be of order 40000. This gives a number density of  $\sim 0.02$  galaxies/Mpc<sup>3</sup>. This method bears some similarities with that used by Jaroszyński.<sup>10) - 11)</sup> Tests showed that the observed galaxy 2-point correlation function is fairly well reproduced (Martel et al.<sup>46)</sup>).

The morphological type of each galaxy is determined by using a combination of the known relations between the present distribution of morphological types and the surface density of galaxies along with a Monte-Carlo method.

The locations of each galaxy at higher redshifts are determined by combining the distribution of the galaxies and that of the particles from the P<sup>3</sup>M simulation, i.e., by following the position of the nearest particle.

We adopt the galaxy models described in Jaroszyński.<sup>10) - 11)</sup> The projected surface density of each galaxy is given by

$$\sigma(r) = \begin{cases} \frac{v^2}{4G(r^2 + r_c^2)^{1/2}}, & r < r_{\max}; \\ 0, & r > r_{\max}, \end{cases} \quad (2.29)$$

where  $r$  is the projected distance from the center. The parameters  $r_c$ ,  $r_{\max}$  and  $v$  are the core radius, maximum radius, and the rotational velocity, respectively. These parameters are functions of the luminosity and morphological types of each galaxy. We assume that the present galaxy luminosities are given by the Schechter luminosity function,

$$n(L)dL = \frac{n_*}{L_*} \left( \frac{L}{L_*} \right)^\alpha e^{-L/L_*} dL, \quad (2.30)$$

where  $n(L)$  is the number density of galaxies per unit luminosity,  $\alpha = -1.10$ ,  $n_* = 0.0156h^3\text{Mpc}^{-3}$ , and  $L_{B*} = 1.3 \times 10^{10}h^{-2}L_\odot$ , where  $L_B$  is the luminosity in the  $B$  band (Efstathiou et al.<sup>47)</sup>). For each galaxy we generate a luminosity  $L$  according to this distribution, and we combine it with the galaxy morphological type to determine the values of the parameters  $v$ ,  $r_c$  and  $r_{\max}$  for that galaxy.

## 2.4. The experiments

### 2.4.1. The cosmological models

We are currently applying the algorithm described above to perform a large cosmological parameter survey. We focus on the CDM model whose density fluctuation power spectrum is described in detail in Bunn and White.<sup>48)</sup> This power spectrum is characterized by 6 independent parameters : (1) the density parameter  $\Omega_0$ ; (2) the contribution  $\Omega_B$  of the baryonic matter to the density parameter; (3) the cosmological constant  $\lambda_0$ ; (4) the Hubble constant  $H_0$ ; (5) the temperature  $T_{\text{CMB}}$  of the cosmic microwave background radiation; and (6) the tilt  $n$  of the power spectrum. We initially set  $T_{\text{CMB}} = 2.7\text{K}$  and  $\Omega_B = 0.015h^{-2}$ , thus reducing the dimensionality of the parameter space to 4. The normalization of the power spectrum is often described in terms of the rms density fluctuation  $\sigma_8$  at a scale of  $8h^{-1}\text{Mpc}$ , which is a function of the 6 aforementioned parameters. We invert this relation, treating  $\sigma_8$  as

an independent parameter, and the tilt  $n$  as the dependent parameter. Presently we have 43 models with various (but restricted) values of the above first 4 parameters.

#### 2.4.2. The ray shooting

In each model we propagate beams of  $341^2$  light rays backward to redshift  $z_s \approx 3$ . The beam has a size of 21.9 arcseconds, and the spacing between rays is 0.064 arcseconds. To analyze the results of the experiments, we lay down grid on the source plane, divided into 31 x 31 cells. Cells which have more than the average number of rays ( $341^2/31^2=121$ ) indicate sources which are magnified. The fraction of such cells gives us the magnification probability. By taking the rays located in such cells, and tracing them back to the image plane, we can study the shape of the images, and in particular, compute the fraction of the magnified sources that have double images. Figure 2 displays a few examples of images of a circular source.

#### 2.5. Preliminary results

We have so far conducted between 30 and 60 ray shooting rays on all of the models, but results of only 35 models have been analyzed. In a previous work (Premadi et al. 1998) we tested the methodology we have described here by studying the statistics of magnification and shear with respect to the lens redshift for a given source redshift. Among other things, we have found that the lensing effect is most prominent at intermediate redshifts although the structures are more evolved at lower redshifts. The redshift where most lensing occurs depends upon the cosmological models. We also show that the magnification is dominated by convergence, with shear contributing less than one part in  $10^4$ .

In the current work we study the magnification probability,  $P_m$ , the probability of double-image events given a lower limit of magnification,  $P_2$ , and the distribution of the separation angle in the double image events.

In Fig. 3, despite the still insufficient statistics, for the majority of models, we observe a tendency for  $P_m$  to decrease with increasing  $\sigma_8$ , and for the cases in which we do not observe this tendency, it is not ruled out because of the large error bars. Having an anticorrelation between  $P_m$  and  $\sigma_8$  is seemingly counter-intuitive, since  $\sigma_8$  measures the amplitude of the density fluctuation, which are responsible for lensing. The explanation is that the magnification is caused primarily by the matter located near the beam, whereas matter located far from the beam are responsible for the shear. In cosmological models like CDM, structure formation proceeds hierarchically. Small structures form first, then merge to form larger structures. A larger  $\sigma_8$  implies that this hierarchical merging process is more advanced. This means that the clusters are more massive, and possibly also denser, but there are fewer of them, thereby enlarging voids between them. The light beam is therefore less likely to hit or pass near any cluster, resulting in a smaller magnification probability for larger  $\sigma_8$ . However, if the beam does hit a cluster, we would expect the effect to be stronger in models with large  $\sigma_8$ , as the clusters are more massive.

In Fig. 4, the plot of  $P_2$  versus  $P_m$  indeed shows an anticorrelation for several models. Another interesting result is that at fixed  $\Omega_0$ ,  $\lambda_0$ , and  $\sigma_8$ , the magnification probability is insensitive to the value of  $H_0$ . This results from the combination of

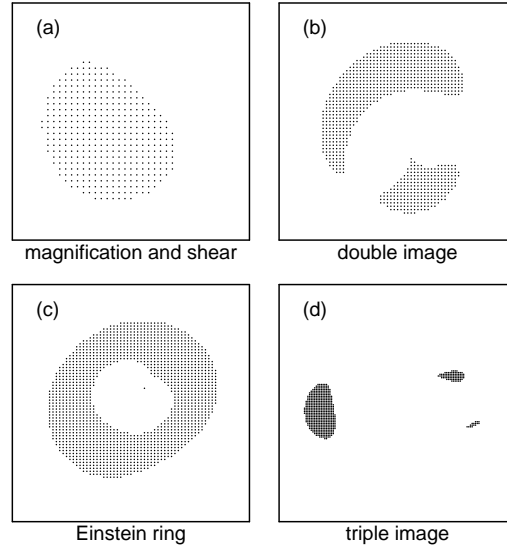


Fig. 2. Various images of circular sources.

two competing effects. On one hand, the number of lens planes between the source and the observer decreases with increasing  $H_0$ . On the other hand, the total mass in each plane is proportional to the critical density, and thus increases with  $H_0$ . Hence, models with larger  $H_0$  have a smaller number of more massive lens-planes.

The histograms of the separation angle (Fig. 5) shows the presence of double peaks in most cases. This seems to be more prominent in the models with larger  $\sigma_8$  when the other cosmological parameters are held fixed. The high density clusters might contain more elliptical galaxies which have smaller cores than the field galaxies. A more compact core is known to result in a larger separation angle. Intriguingly,

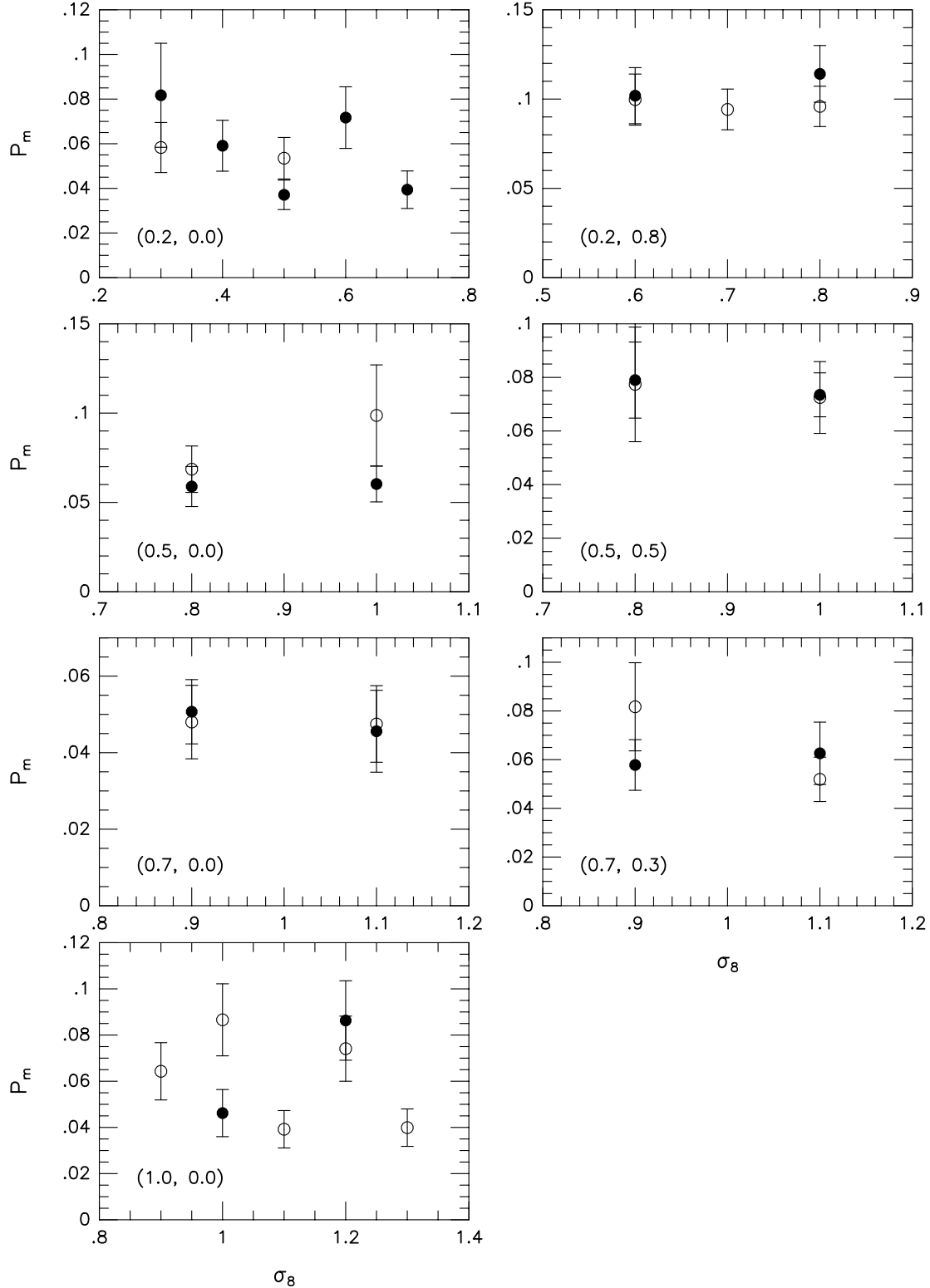


Fig. 3. Magnification probability  $P_m$  of magnification 1.2 and larger as a function of the rms density fluctuation  $\sigma_8$ . The numbers in parentheses indicate the values of  $(\Omega_0, \lambda_0)$ . Open circles

Fig. 4. Multi-image probability  $P_2$  as a function of magnification probability  $P_m$ . The numbers in parentheses indicate the values of  $(\Omega_0, \lambda_0)$ . Open circles correspond to  $H_0 = 65$  and circles to  $H_0 = 75$ .

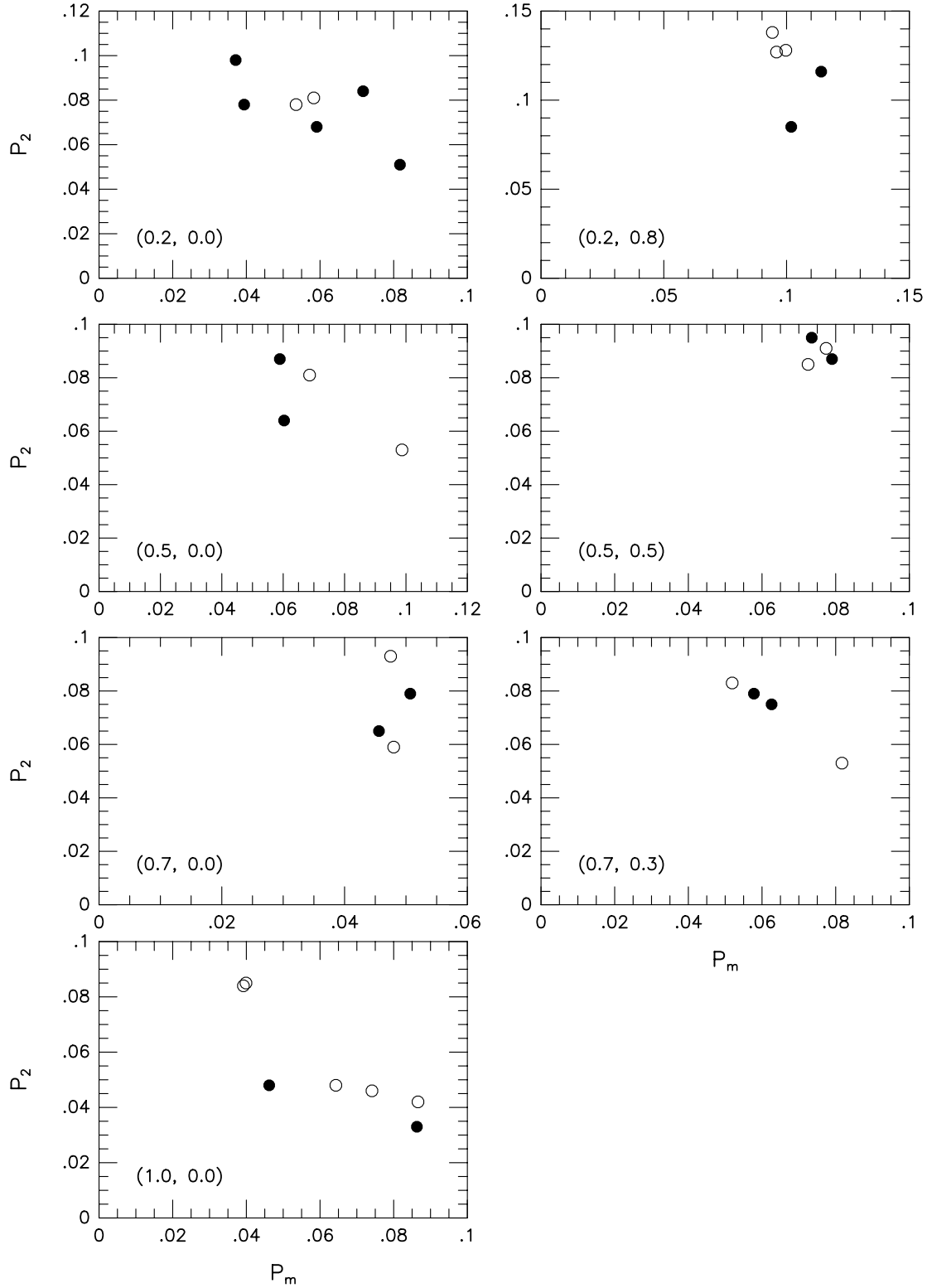
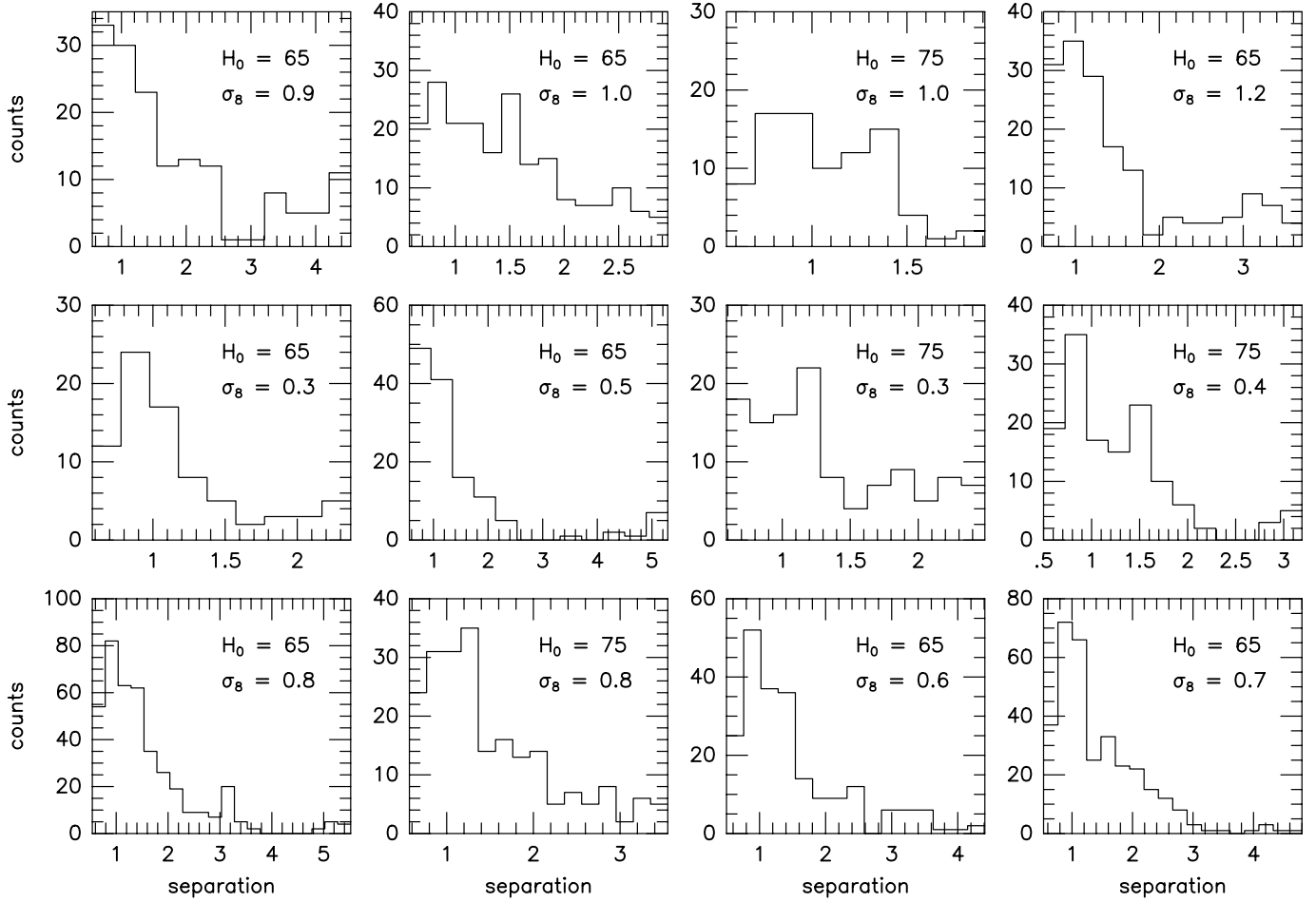


Fig. 5. The distribution of the image separation in arc seconds. The counts are not normalized to the numbers of runs which are not the same for all models. Top row displays results for models with  $\Omega_0 = 1.0$ ,  $\lambda_0 = 0.0$ . The middle row for models with  $\Omega_0 = 0.2$ ,  $\lambda_0 = 0.0$ , and the bottom row for models with  $\Omega_0 = 0.2$ ,  $\lambda_0 = 0.8$ .



models with smaller  $H_0$  seem to produce longer high separation tails. The presence of  $\lambda_0$  also seems to stretch the histogram to a higher separation tail, although by a smaller amount than that caused by high  $\sigma_8$ . In addition to this, it also increases the counts at mid-separation. This might indicate that structures in  $\lambda_0$  models have large sizes which are responsible for midsize separation angles.

Even at this preliminary stage, the results show the different tendencies among various cosmological models. With better statistics, we are hopeful that the differences can be sharpened, and that these differences will eventually enable us to make meaningful comparisons with observational results, thereby discriminating the cosmological models.

### §3. Cosmological lensing in the direct integration method

In this section we study the behavior of light ray bundles in inhomogeneous model universes, solving directly the null geodesic equation in the (cosmological) Newtonian approximation at the stage from an epoch  $t_1$  (with redshift  $z_1 = 5$ ) to the present epoch  $t_0$ . Light rays are deflected by lens objects such as galaxies and non-galactic clouds. Here, these clouds are mass concentrations which are unilluminous but have masses comparable with a standard galactic mass. It is not clear at present what average mass and size and what number density such clouds have, compared with those of galaxies. In some previous papers (by Tomita<sup>31)–32)</sup>, we assumed that non-galactic clouds are dominant and have a standard galactic mass and lensing strength similar to that of galaxies. In this paper we consider another case, in which only galaxies are dominant lenses and all non-galactic clouds are very weak lenses, and compare the results concerning optical deformations in this case with those in the previous case. In the future observations about the shear deformation at small angles will provide the information for the structure and lensing strength of non-galactic clouds.

#### 3.1. Model universes and the ray shooting

The background model universes have the line-element

$$ds^2 = -(1 + 2\varphi/c^2)c^2 dt^2 + (1 - 2\varphi/c^2)a^2(t)(d\mathbf{x})^2/[1 + K\frac{1}{4}(\mathbf{x})^2]^2, \quad (3.1)$$

where  $K$  is the signature of spatial curvature ( $\pm 1, 0$ ). The normalized scale factor  $S \equiv a(t)/a(t_0)$  satisfies

$$\left(\frac{dS}{d\tau}\right)^2 = \frac{1}{S} \left[ \Omega_0 - (\Omega_0 + \lambda_0 - 1)S + \lambda_0 S^3 \right], \quad (3.2)$$

where  $\tau \equiv H_0 t$  and  $a_0 (\equiv a(t_0))$  is specified by the relation  $(cH_0^{-1}/a_0)^2 = 1 - \Omega_0 - \lambda_0$ . The gravitational potential  $\varphi$  is described by the Poisson equation

$$\begin{aligned} a^{-2} \Delta \varphi &= \left[ 1 - \frac{1}{4}(\mathbf{x})^2 \right]^2 \left[ \frac{\partial^2 \varphi}{\partial \mathbf{x}^2} + \frac{\frac{1}{2}x^i}{[1 + K\frac{1}{4}(\mathbf{x})^2]^3} \frac{\partial \varphi}{\partial x^i} \right] \\ &= 4\pi G \rho_B [\rho(\mathbf{x})/\rho_B - 1], \end{aligned} \quad (3.3)$$

where  $\rho_B (= \rho_{B0}/S^3)$  is the background density and

$$\rho_{B0} = \frac{3H_0^2 \Omega_0}{8\pi G} = 2.77 \times 10^{11} \Omega_0 h^2 M_\odot \text{ Mpc}^{-3}, \quad (3.4)$$

where  $H_0 = 100h \text{ Mpc}^{-1} \text{ km s}^{-1}$ . In our treatment the inhomogeneities are locally periodic in the sense that the physical situation at  $\mathbf{x}$  is the same as that at  $\mathbf{x} + l\mathbf{n}$ , where the components of  $\mathbf{n} (= (n^1, n^2, n^3))$  are integers. In an arbitrary periodic box with coordinate volume  $l^3$ , there are  $N$  particles with the same mass  $m$ . It is assumed that the force at an arbitrary point is the sum of forces from  $N$  particles in the box whose center is the point in question, and that the forces from outside the box can be neglected.

In this subsection we consider two flat models (S model and L model) with  $(\Omega_0, \lambda_0) = (1.0, 0)$  and  $(0.2, 0.8)$ , respectively, and an open model (O model) with  $(0.2, 0)$ . The present lengths of the boxes are

$$L_0 \equiv a(t_0)l = 32.5h^{-1}, 50h^{-1}, 50h^{-1} \text{ Mpc} \quad (3.5)$$

for S, L and O models, respectively. The particle number is  $32^3$  in all models, and thus

$$m (= \rho_{B0} L_0^3 / N) = 2.90, 2.11, 2.11 \times 10^{11} h^{-1} M_\odot, \quad (3.6)$$

respectively.

The distributions of particles in these models were derived using numerical  $N$ -body simulations. The particle size (giving the lens strength) is represented by the softening radius  $r_s (= a(t)x_s)$ , which is constant. For the particle size we consider two lens models for comparison:

**Lens model 1.** All particles in the low-density models ( $\Omega_0 = 0.2$ ) have  $r_s = 20h^{-1} \text{ kpc}$ , 20% of the particles in the flat model  $(1.0, 0)$  have  $r_s = 20h^{-1} \text{ kpc}$ , and the remaining particles have  $r_s = 500h^{-1} \text{ kpc}$ . Thus practically, particles with  $\Omega_c = 0.2$  (which we call *compact lens objects* in previous papers<sup>31)–32)</sup> play the role of lens objects. Their number density is much larger than the galactic density  $\Omega_g \sim 0.02$ .

**Lens model 2.** 10% of the particles in the low-density model ( $\Omega_0 = 0.2$ ) and 2% of the particles in the flat model  $(1.0, 0)$  have  $r_s = 20h^{-1} \text{ kpc}$ , while the remaining particles have  $r_s = 500h^{-1} \text{ kpc}$ . Thus only galaxies corresponding to  $\Omega_g = 0.02$  play significant roles as lens objects, and the remaining particles are regarded as diffuse clouds.

The lens strength of realistic non-galactic clouds is intermediate between these two lens models. The question of which model is better may be answered by observational studies involving lens phenomena.

The time evolution of the distribution of particles was derived by performing the  $N$ -body simulation in the tree-code provided by Suto.<sup>49)</sup> The initial particle distributions were derived using Bertschinger's software *COSMICS*<sup>50)</sup> under the condition that their perturbations are given as random fields with the spectrum of cold dark matter, their power  $n$  is 1, and their normalization is specified as the dispersion  $\sigma_8 = 0.94$  with the Hubble constant  $h = 0.5$  for  $(1.0, 0)$  and  $h = 0.7$  for other models with  $\Omega_0 = 0.2$ .



Now let us consider light propagation described by the null geodesic equation with the null condition. Here we use  $T \equiv \frac{1}{2} \ln[a(t)/a(t_1)]$  as a time variable and  $T_0 \equiv (T)_{t=t_0}$ . Then we have  $dS = 2 \exp[2(T - T_0)]dT$ , so that

$$cdt = R c_R [\Omega_0 + (1 - \Omega_0 - \lambda_0)S + \lambda_0 S^3]^{-1/2} e^{3T} dT, \quad (3.7)$$

where

$$R \equiv L_0 / [(1 + z_1)N^{1/3}] \quad (3.8)$$

and

$$c_R \equiv 2(c/H_0) / [R(1 + z_1)^{3/2}]. \quad (3.9)$$

The line-element is

$$ds^2/R^2 = -c_R^2 [\Omega_0 + (1 - \Omega_0 - \lambda_0)S + \lambda_0 S^3]^{-1} e^{6T} (1 + \alpha\phi) dT^2 + (1 - \alpha\phi) e^{4T} d\mathbf{y}^2 / F(\mathbf{y})^2, \quad (3.10)$$

where  $y^0 \equiv T$ ,  $y^i \equiv a(t_1)x^i/R$ ,  $\varphi \equiv (Gm/R)\phi$ ,  $R_0 \equiv Ra_0/a_1 = (1 + z_1)R$ ,

$$\alpha \equiv \frac{2Gm}{c^2 R} = \frac{3}{\pi} \frac{\Omega_0}{(c_R)^2} \quad (3.11)$$

and

$$F \equiv 1 - \frac{1}{4} (R_0 H_0 / c)^2 (1 - \Omega_0 - \lambda_0) (\mathbf{y})^2. \quad (3.12)$$

The equations to be solved for light rays are

$$\frac{dy^i}{dT} = c_R e^T \tilde{K}^i, \quad (3.13)$$

$$\begin{aligned} \frac{d\tilde{K}^i}{dT} = & - [3\lambda_0 e^{4(T-T_0)} + (1 - \Omega_0 - \lambda_0)] e^{2(T-T_0)} \tilde{K}^i / G(T) + \alpha \frac{\partial\phi}{\partial T} \tilde{K}^i \\ & - \gamma c_R^{-1} e^T \left[ \partial\phi / \partial y^i / G(T) - 2 \frac{\partial\phi}{\partial y^j} \tilde{K}^j \tilde{K}^i \right] \\ & + (R_0 H_0 / c)^2 (1 - \Omega_0 - \lambda_0) F^{-1} c_R e^T \\ & \times \left[ -y^j \tilde{K}^j \tilde{K}^i + \frac{1}{2} (1 + 2\alpha\phi) / G(T) \right], \end{aligned} \quad (3.14)$$

where  $\tilde{K}^i \equiv c_R^{-1} e^{-T} dy^i / dT$ ,  $\gamma \equiv \alpha (c_R)^2$  and

$$G(T) = \Omega_0 + (1 - \Omega_0 - \lambda_0) e^{2(T-T_0)} + \lambda_0 e^{6(T-T_0)}. \quad (3.15)$$

The null condition is

$$\sum_i (\tilde{K}^i)^2 = 1 + 2\alpha\phi. \quad (3.16)$$

While in flat models the solution is straightforward, some care must be taken in curved models. The potential  $\phi$  is given as a solution of the Poisson equation. Because the ratio of the second term to the first term on the right-hand side of Eq.

(3.3) is  $(R_0 H_0 / c)^2 (\mathbf{y})^2 [\Delta y / |\mathbf{y}|] \ll 1$  for  $z \leq z_1$ , the Poisson equation in a box can be approximately expressed as

$$F(\mathbf{y}_c)^2 \frac{\partial^2 \phi}{\partial \mathbf{y}^2} = 4\pi G \rho_B [\rho(\mathbf{x}) / \rho_B - 1], \quad (3.17)$$

where we have used  $F(\mathbf{y}) \simeq 1$  for  $y \sim$  [the box size].  $F(\mathbf{y})$  can be approximately replaced by the central value  $F(\mathbf{y}_c)$  for  $y \gg$  [the box size], where the index  $c$  denotes the central value in the box. For point sources with  $\rho = m \sum_n \delta(aR(\mathbf{y} - \mathbf{y}_n))$  ( $n$  is the particle number), we have  $\phi = \phi_1 + \phi_2$ , where

$$\phi_1 = -F(\mathbf{y}_c) e^{-2T} \sum_n \frac{1}{|\mathbf{y} - \mathbf{y}_n|}, \quad (3.18)$$

and  $\phi_2$  represents the contribution from the homogeneous background density. Here let us use for  $\mathbf{y}$  another vectors  $\bar{\mathbf{y}}$  expressing the space in a locally flat manner, where the two coordinates are related as

$$\bar{\mathbf{y}} = \int_0^{\mathbf{y}} d\mathbf{y} / F(\mathbf{y}), \quad (3.19)$$

and the lengths between two points in boxes in two coordinates are approximately related as

$$\Delta \bar{\mathbf{y}} = \Delta \mathbf{y} / F(\mathbf{y}_c). \quad (3.20)$$

Then  $\phi_1$  can be expressed in terms of  $\bar{\mathbf{y}}$  in the usual manner as

$$\phi_1 = -e^{-2T} \sum_n \frac{1}{|\bar{\mathbf{y}} - \bar{\mathbf{y}}_n|}. \quad (3.21)$$

Corresponding forces are expressed as  $f_i \equiv \partial \phi_1 / \partial y^i = [\partial \phi_1 / \partial \bar{y}^i] / F(\mathbf{y}_c)$ . It should be noted that the contribution of  $\partial \phi / \partial T$  is negligibly small, compared with that of  $f_i$ .

In flat models the universe is everywhere covered with periodic boxes continuously connected as in Fig. 6. In open models it cannot be covered in such a way, but we can consider only a set of local periodic boxes connected along each light ray, as in Fig. 7. In these boxes we can describe the evolution in the distribution of particles in terms of local flat coordinates  $\bar{\mathbf{y}}$ , because the size of boxes is much smaller than the curvature radius.

For the integration of the above null-geodesic equations, we calculate the potential at a finite number of points on the ray which are given at each time step ( $\Delta T$ ). Then particles near one of the points on the ray have a stronger influence upon the potential than particles far from any points. To avoid this unbalance in the calculation of the potential, we take an average of the potential  $\phi_1$  by integrating it analytically over the interval between one of the points and the next point. The expression for an averaged potential  $\bar{\phi}$  was given in a previous paper. Moreover, to take into account the finite particle size as galaxies or non-galactic clouds, we modify the above potential for point sources using the softening radii  $y_s = a(t_1) x_s / R$ . The

modified potential is produced by replacing  $(y - y_n)^2$  by  $(y - y_s)^2 + (y_s)^2$  in the potential for point sources.

The initial values of  $\tilde{K}^i$  are given so as to satisfy Eq. (3.16). The integration of Eqs. (3.13) and (3.14) with the modified potential was performed using the Adams method. As the time step we used  $\Delta T = [\ln 6/2]/N_s$  with  $N_s = 3000$  (in most cases)  $-10000$ .

Here we consider the comoving volume of the region through which a ray bundle with solid angle  $\theta^2$  pass at the interval  $0 \leq z \leq z_i$  in the flat model (1.0, 0). This volume is equal to the volume of the cone  $V_R = \frac{1}{3}\theta^2 [2cH_0(1 - 1/\sqrt{1+z_i})]^3$ . Its ratio to the volume of the periodic box  $V_B [= (32h^{-1}\text{Mpc})^3]$  is  $1.2 \times 10^{-3}$  for  $z_i = 5$  and  $\theta = 10\text{arcsec}$ . This small ratio implies that the influence of the periodicity of the box on the the statistics of ray bundles is negligibly small, as long as the ray bundles are not directed in some special directions with respect to the box.

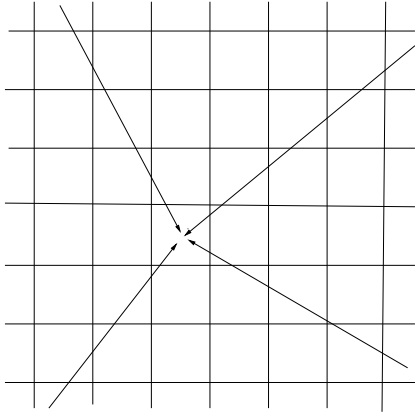


Fig. 6. Light rays and periodic boxes in a flat space.

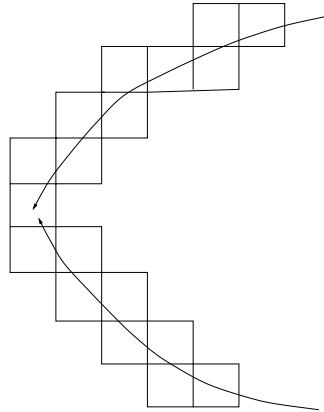


Fig. 7. Light rays and periodic boxes in an open space.

### 3.2. Statistical behavior of optical scalars

We treat the deformation of ray bundles over the interval from  $z = 0$  to  $z = 5$  measured by an observer in a periodic box. Here we consider the ray bundles reaching the observer (or emitted backwards) in a regular form such that the rays are put in the same separation angle  $\theta$ , and calculate the relative change in the angular positions of the rays which increases with redshift in the past direction. From this change we find the behavior of optical scalars.

Basic ray bundles consist of  $5 \times 5$  rays that are put in a square form with the same separation angle  $\theta = 2 - 360$  arcsec. Many bundles coming from all directions in the sky are considered. Here we take 200 bundles coming from randomly chosen directions for each separation angle. In order to express relative angular positions of rays, we use two orthogonal vectors,  $e_{(1)}^i$  and  $e_{(2)}^i$ , in the plane perpendicular to the first (fiducial) background ray vector  $(\tilde{K}^i)_B$ . Then the angular coordinates  $[X(m, n), Y(m, n)]$  of 25 rays relative to the first (fiducial) ray with  $(m, n) = (1, 1)$

at any epoch are defined by

$$\begin{aligned} X(m, n) &= \sum_i [y^i(m, n) - y^i(1, 1)] e_{(1)}^i / y_B(1, 1) + X(1, 1), \\ Y(m, n) &= \sum_i [y^i(m, n) - y^i(1, 1)] e_{(2)}^i / y_B(1, 1) + Y(1, 1), \end{aligned} \quad (3.22)$$

where  $y^i = y_B^i + \delta y^i$  and  $y_B = [\sum_i (y_B^i)^2]$ . Since all angular intervals of rays at the observer's point are the same ( $= \theta$ ), the differentiation of angular coordinates of the rays at any epoch with respect to those at the observer's points is given by the differences

$$\begin{aligned} A_{11}(m, n) &= [X(m+1, n) - X(m, n)] / \theta, \\ A_{12}(m, n) &= [X(m, n+1) - X(m, n)] / \theta, \\ A_{21}(m, n) &= [Y(m+1, n) - Y(m, n)] / \theta, \\ A_{22}(m, n) &= [Y(m, n+1) - Y(m, n)] / \theta, \end{aligned} \quad (3.23)$$

where  $m$  and  $n$  run from 1 to 5. From the matrix  $A_{ij}(m, n)$  we derive the optical scalars in the standard manner,<sup>5)</sup> as the convergence ( $\kappa(m, n)$ ), the shear ( $\gamma_i(m, n)$ ,  $i = 1, 2$ ), and the amplification ( $\mu(m, n)$ ) defined by

$$\begin{aligned} \kappa(m, n) &= 1 - \text{tr}(m, n) / 2, \quad \gamma_1(m, n) = [A_{22}(m, n) - A_{11}(m, n)] / 2, \\ \gamma_2(m, n) &= -[A_{12}(m, n) + A_{21}(m, n)] / 2, \\ \gamma^2 &\equiv (\gamma_1)^2 + (\gamma_2)^2 = [\text{tr}(m, n)]^2 - \det(A_{ij}(m, n)), \\ \mu(m, n) &= 1 / \det(A_{ij}(m, n)), \end{aligned} \quad (3.24)$$

where the trace is  $\text{tr}(m, n) = A_{11}(m, n) + A_{22}(m, n)$ . The average optical quantities in each bundle are defined as the averages of optical quantities for all rays in the bundle as

$$\bar{\kappa} = \left[ \sum_m \sum_n \kappa(m, n) \right] / 4^2, \quad \bar{\kappa}^2 = \left[ \sum_m \sum_n (\kappa(m, n))^2 \right] / 4^2, \quad (3.25)$$

and so on. In this averaging process the contributions from smaller scales can be cancelled and smoothed-out. The above optical scalars at the separation angle  $\theta$  are accordingly derived in the coarse-graining on this smoothing scale.

For the present statistical analysis we excluded caustic cases, considering only the case of *weak lensing* in the sense of *no caustics*. The averaging for all non-caustic ray bundles is denoted using  $\langle \rangle$  as  $\langle \kappa^2 \rangle$ ,  $\langle \gamma^2 \rangle$  and  $\langle (\mu - 1)^2 \rangle$ . Because  $\kappa(m, n)$ ,  $\gamma_i(m, n)$  and  $\mu(m, n) - 1$  take positive and negative values with almost equal frequency,  $\langle \kappa \rangle$ ,  $\langle \gamma_i \rangle$  and  $\langle \mu \rangle - 1$  are small.

In Figs. 8 and 9, we show the behavior of  $\langle \gamma^2 \rangle$  for various separation angles  $\theta = 2 \text{ arcsec} - 360 \text{ arcsec}$  ( $= 6 \text{ arcmin}$ ) at epochs  $z = 1.0$  and  $2.0$ , respectively. Similarly in Figs. 10 and 11, we show the behavior of  $\langle (1 - \mu)^2 \rangle$  at epochs  $z = 1.0$  and  $2.0$ , respectively. The calculations were performed at  $\theta = 2, 5, 10, 30, 60$ , and  $360 \text{ arcsec}$ . The behavior of  $\langle \kappa^2 \rangle$  is similar to that of  $\langle \gamma^2 \rangle$ , as was shown in previous papers. In all figures, the values in the two lens models are shown using solid and dotted lines. It is found in the low-density models that the ratios of  $\langle \kappa^2 \rangle^{1/2}$ ,  $\langle \gamma^2 \rangle^{1/2}$

and  $\langle(1 - \mu)^2\rangle^{1/2}$  in the lens model 1 to those in the lens model 2 are about 4 at the separation angle  $\theta = 2$  arcsec. The ratios decrease with the increase of  $\theta$ , and are  $< 2$  at  $\theta = 360$  arcsec. That is, the remarkable difference between the two lens models appears at the small angles  $\theta \simeq 2$  arcsec. The values of optical scalars for  $\theta \sim 360$  arcsec are roughly consistent with the results of Bernardeau et al. (cf. their Figs. 3 and 4)<sup>37)</sup> and Nakamura<sup>38)</sup> in their treatments.

At all separation angles and for both lens models,  $\langle\kappa^2\rangle$ ,  $\langle\gamma^2\rangle$  and  $\langle(1 - \mu)^2\rangle$  in the open model ( $\Omega_0 = 0.2$ ) are larger than those in the flat model (L). In model S they are largest at all angles for the lens model 2 and at large angles ( $\theta \sim 360$  arcsec) in the lens model 1, but they are smallest at small angles ( $\theta < 30$  arcsec) because the role of non-galactic clouds on small-scale is small.

In Tables I, II and III, we show for models S, L and O the numerical values of  $\langle\kappa\rangle$ ,  $\langle\kappa^2\rangle^{1/2}$ ,  $\langle\mu\rangle$ ,  $\langle(\mu - 1)^2\rangle^{1/2}$ ,  $\langle\gamma_1\rangle$  and  $\langle\gamma^2\rangle^{1/2}$  at epochs  $z = 1, 2, \dots, 5$  for  $\theta = 2$  arcsec.

The influence of lensing on source magnitudes is

$$\Delta m = \frac{5}{2} \log[1 + \langle(1 - \mu)^2\rangle^{1/2}] \simeq 1.09 \langle(1 - \mu)^2\rangle^{1/2}. \quad (3.26)$$

If  $\theta = 2$  arcsec, the value of  $\Delta m$  is (0.058, 0.034), (0.077, 0.019) and (0.133, 0.022) for the lens model (1, 2), respectively, at  $z = 1$  in models S, L and O. If the lens model 1 is more realistic, therefore, this lens correction may introduce some sensitive modification to the standard selection of cosmological models in the  $[m, z]$  relation. Here it should be noted that the lensing effect at small angles, which is caused by small-scale nonlinear inhomogeneities, is important for the magnitude correction of small high-redshift objects, such as SNe Ia, in cosmological observations.<sup>51) - 52)</sup>

Table I. Optical quantities in model S at  $\theta = 2$  arcsec.

<i>lens</i>	<i>z</i>	$\langle\kappa\rangle$	$\langle\kappa^2\rangle^{1/2}$	$\langle\mu\rangle$	$\langle(1 - \mu)^2\rangle^{1/2}$	$\langle\gamma_1\rangle$	$\langle\gamma^2\rangle^{1/2}$
1	1	0.0005	0.0245	1.0036	0.0529	-0.0032	0.0251
	2	0.0004	0.0398	1.0075	0.0858	-0.0061	0.0409
	3	0.0021	0.0495	1.0149	0.1084	-0.0080	0.0514
	4	0.0034	0.0563	1.0208	0.1251	-0.0096	0.0593
	5	0.0042	0.0617	1.0253	0.1390	-0.0109	0.0653
2	1	0.0005	0.0155	1.0020	0.0315	-0.0026	0.0152
	2	0.0020	0.0251	1.0065	0.0516	-0.0049	0.0238
	3	0.0030	0.0305	1.0096	0.0636	-0.0053	0.0283
	4	0.0037	0.0343	1.0120	0.0721	-0.0055	0.0314
	5	0.0041	0.0370	1.0136	0.0784	-0.0055	0.0339

For the statistical analysis we used 200 ray bundles reaching an observer in a single inhomogeneous model universe. This number of ray bundles may be too small to cover the influences from complicated inhomogeneities in all directions. To obtain more robust statistical results it may be necessary to use more ray bundles and more model universes produced with random numbers.

Finally, we touch upon recent observations of cosmological shear due to weak lensing and their relation to our results. Fort et al.<sup>53)</sup> attempted measurements of a coherent shear from foreground mass condensations in the fields of several luminous

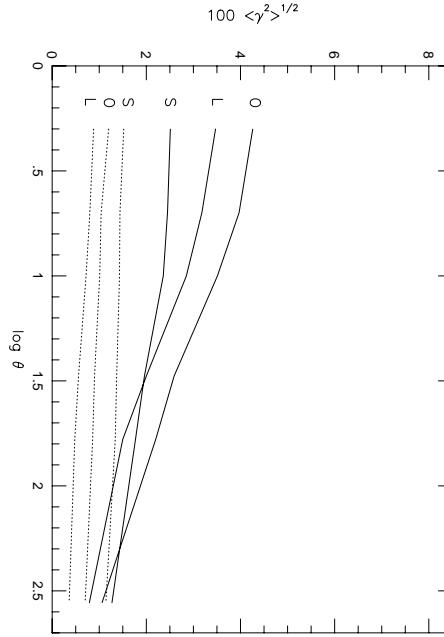


Fig. 8. The angular dependence of  $\langle \gamma^2 \rangle^{1/2}$ . Solid and dotted lines represent behavior for lens models 1 and 2, respectively, at  $z = 1$ . The separation angle  $\theta$  is in units of arcsec.

Table II. Optical quantities in model L at  $\theta = 2$  arcsec.

<i>lens</i>	<i>z</i>	$\langle \kappa \rangle$	$\langle \kappa^2 \rangle^{1/2}$	$\langle \mu \rangle$	$\langle (1 - \mu)^2 \rangle^{1/2}$	$\langle \gamma_1 \rangle$	$\langle \gamma^2 \rangle^{1/2}$
1	1	-0.0011	0.0324	1.0025	0.0705	0.0008	0.0347
	2	-0.0036	0.0675	1.0134	0.1572	0.0018	0.0714
	3	-0.0045	0.0974	1.0345	0.2407	0.0020	0.1002
	4	-0.0065	0.1216	1.0560	0.3209	0.0023	0.1214
	5	-0.0070	0.1405	1.0805	0.4000	0.0030	0.1372
2	1	0.0001	0.0084	1.0004	0.0174	-0.0004	0.0088
	2	0.0004	0.0175	1.0021	0.0367	-0.0018	0.0180
	3	0.0001	0.0239	1.0025	0.0505	-0.0020	0.0245
	4	0.0001	0.0291	1.0038	0.0618	-0.0019	0.0296
	5	0.0005	0.0333	1.0055	0.0710	-0.0017	0.0334

radio sources. Schneider et al.<sup>54)</sup> determined the shear in the field ( $2 \text{ min} \times 2 \text{ min}$ ) containing a radio source PKS1508-05 with  $z = 1.2$ , and their result is that the shear is about 0.03 for an angular scale of 1 min. This value may be consistent with the low-density models in the lens model 1, but more observational data are necessary to deduce any conclusions. In order to clarify the lensing strength of non-galactic clouds it is important to have observational values of the shear at small angles  $\theta \approx 2$  arcsec.

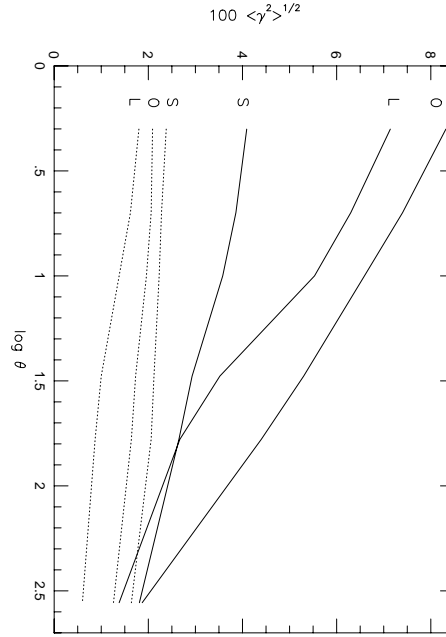


Fig. 9. The angular dependence of  $\langle \gamma^2 \rangle^{1/2}$ . Solid and dotted lines denote behavior for lens models 1 and 2, respectively, at  $z = 2$ . The separation angle  $\theta$  is in the unit of arcsec.

Table III. Optical quantities in model O at  $\theta = 2$  arcsec.

<i>lens</i>	$z$	$\langle \kappa \rangle$	$\langle \kappa^2 \rangle^{1/2}$	$\langle \mu \rangle$	$\langle (1 - \mu)^2 \rangle^{1/2}$	$\langle \gamma_1 \rangle$	$\langle \gamma^2 \rangle^{1/2}$
1	1	-0.0002	0.0425	1.0221	0.1219	-0.0028	0.0426
	2	-0.0054	0.0796	0.9961	0.2210	-0.0041	0.0832
	3	-0.0069	0.1157	1.0368	0.6234	0.0057	0.1225
	4	-0.0081	0.1519	1.0790	0.5638	0.0078	0.1602
	5	-0.0064	0.1872	1.1627	1.1880	0.0120	0.1980
2	1	-0.0003	0.0099	0.9997	0.0205	-0.0005	0.0120
	2	-0.0012	0.0209	0.9993	0.0441	-0.0015	0.0209
	3	0.0000	0.0314	1.0041	0.0682	-0.0035	0.0284
	4	0.0010	0.0410	1.0089	0.0915	-0.0047	0.0370
	5	0.0021	0.0496	1.0144	0.1140	-0.0059	0.0451

#### §4. Analytic evaluation of cosmic shear through the power spectrum approach <sup>\*)</sup>

In this section we analytically estimate the shear and the image amplification caused by large scale density inhomogeneity in the universe.<sup>2) 34) - 38)</sup> emanating from us to the past, and let  $\chi$  be the affine parameter along the central ray in the

<sup>\*)</sup> In this section we use units in which  $c = H_0 = 1$  and follow Misner et al.<sup>55)</sup> as regards the sign convention of curvature tensors.

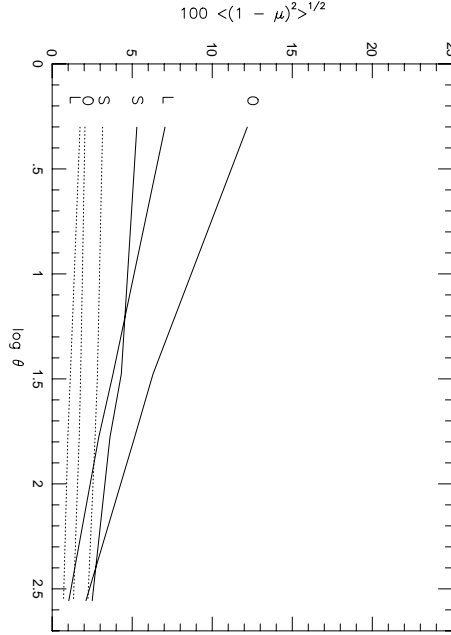


Fig. 10. The angular dependence of  $\langle (1 - \mu)^2 \rangle^{1/2}$ . Solid and dotted lines represent behavior for lens models 1 and 2, respectively, at  $z = 1$ . The separation angle  $\theta$  is in units of arcsec.

bundle and  $k^a = (d/d\chi)^a$  be its tangent vector. Deformation in the cross section of the bundle is described by optical scalars, the expansion  $\theta = \frac{1}{2}\nabla_a k^a$  and shear  $\sigma = \frac{1}{2}\epsilon^a \epsilon^b \nabla_a k_b$ , where  $\epsilon^a = e_1^a + ie_2^a$  is the complex dyad basis on the cross section. The rotation  $\omega = \frac{1}{2}\text{Im}(\epsilon^{*a}\epsilon^b)\nabla_a k_b$  identically vanishes for a bundle which emanates from a single point, so we set  $\omega = 0$  in the following. These evolve along the ray according to the equations<sup>5), 63)</sup>

$$\dot{\theta} + \theta^2 + |\sigma|^2 = -\mathcal{R}, \quad \dot{\sigma} + 2\theta\sigma = -\mathcal{F}, \quad (4.1)$$

where the overdot denotes  $d/d\chi$ , and the sources of deformation are  $\mathcal{R} = \frac{1}{2}R_{ab}k^a k^b$  and  $\mathcal{F} = \frac{1}{2}C_{abcd}\epsilon^a \epsilon^b k^c k^d$ . The observable effect of this deformation is the evolution of a deviation vector  $\xi^a$  connecting two nearby rays on the cross section:

$$\dot{\xi} = \theta\xi + \sigma\xi^*. \quad (4.2)$$

where  $\xi = \epsilon_a \xi^a$ . This deviation vector is written as a linear mapping from the initial value of  $\dot{\xi}$  at  $\chi = 0$ :

$$\xi = \Lambda^* \dot{\xi}_0 + \Gamma \dot{\xi}_0^*. \quad (4.3)$$

Here  $\dot{\xi}_0$  represents the angular separation between the nearby rays in the observer's sky, and  $\text{Re}\Lambda$ ,  $\text{Im}\Lambda$  and  $\Gamma$  represent respectively the degrees of focusing, rotation and shear in the shape of the cross section as seen from the observer. From equation



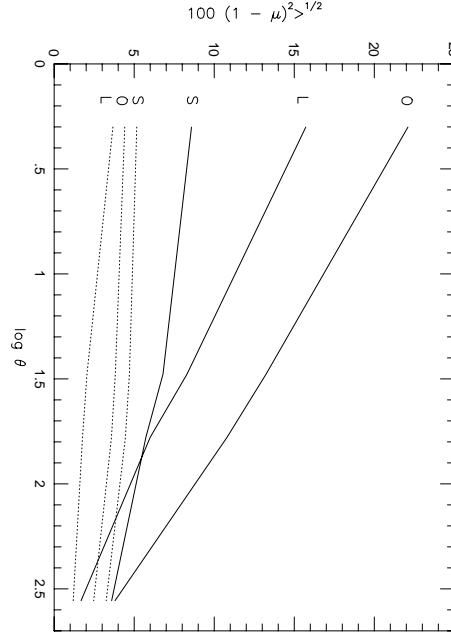


Fig. 11. The angular dependence of  $\langle(1 - \mu)^2\rangle^{1/2}$ . Solid and dotted lines represent behavior for lens models 1 and 2, respectively, at  $z = 2$ . The separation angle  $\theta$  is in the unit of arcsec.

(4.1) it follows that

$$\dot{\Lambda} = \theta\Lambda + \sigma^*\Gamma, \quad \ddot{\Lambda} = -(\mathcal{R}\Lambda + \mathcal{F}^*\Gamma), \quad (4.4)$$

$$\dot{\Gamma} = \sigma\Lambda + \theta\Gamma, \quad \ddot{\Gamma} = -(\mathcal{F}\Lambda + \mathcal{R}\Gamma). \quad (4.5)$$

The angular diameter distance  $D$  is defined to be (cross sectional area/solid angle in the sky) $^{1/2}$  so  $D = (|\Lambda|^2 - |\Gamma|^2)^{1/2}$  and satisfies

$$\dot{D} = \theta D, \quad \ddot{D} = -(\mathcal{R} + |\sigma|^2)D. \quad (4.6)$$

Initial conditions for these differential equations at  $\chi = 0$  are  $0 = \Lambda = \Gamma = \dot{\Gamma} = D = \sigma$  and  $\dot{\Lambda} = \dot{D} = 1$ .

The following form of the metric is used to describe the globally homogeneous but locally inhomogeneous universe

$$d\hat{s}^2 = a^2 ds^2 = a^2(\eta) [-(1 + 2\Phi)d\eta^2 + (1 - 2\Phi)\gamma_{ij}dx^i dx^j]. \quad (4.7)$$

Here  $a$  is the scale factor and  $\gamma_{ij}$  is the 3-metric on the constant time hypersurface of curvature  $K = \Omega_0 + \lambda_0 - 1$ . The gravitational potential  $\Phi$  ( $\ll 1$ ) incorporates the local inhomogeneity generated by the density contrast  $\delta = (\rho - \bar{\rho})/\bar{\rho}$  and satisfies the Poisson equation

$$\nabla^2\Phi = \frac{3}{2}\Omega_0\frac{\delta}{a}, \quad (4.8)$$

where  $\nabla^2$  is the Laplacian associated with  $\gamma_{ij}$  (we only consider a sub-horizon scale inhomogeneity whose wavelength is much smaller than  $|K|^{-1/2}$ ). Since the null geodesics are unaffected by the conformal transformation, we work in the scaled metric  $ds^2$  in what follows. Accordingly the ‘‘distances’’  $\hat{\Lambda}$  and  $\hat{T}$  (Eq.(4.3)) in the metric  $d\hat{s}^2$  are related to those in  $ds^2$  as  $\hat{\Lambda} = a\Lambda$  and  $\hat{T} = a\Lambda$ . The affine parameter  $\chi$  is related to the redshift  $z = 1/a - 1$  as

$$\chi(z) = \int_a^1 dx (\Omega_0 x - Kx^2 + \lambda_0 x^4)^{-1/2}. \quad (4.9)$$

From Eq. (4.7) we obtain  $\mathcal{R} = K + \nabla^2\Phi$  and  $\mathcal{F} = \epsilon^i\epsilon^j\nabla_i\nabla_j\Phi$ . We regard  $\delta\mathcal{R} = \nabla^2\Phi$  and  $\delta\mathcal{F} = \epsilon^i\epsilon^j\nabla_i\nabla_j\Phi$  as perturbations to  $\bar{\mathcal{R}} = K$  and  $\bar{\mathcal{F}} = 0$ , and solve Eqs. (4.4) and (4.5) perturbatively. The zeroth order solution in an exactly homogenous universe is

$$\bar{\Lambda}(\chi) = \bar{D}(\chi) = \begin{cases} K^{-1/2} \sin(K^{1/2}\chi), & (K > 0) \\ \chi, & (K = 0) \\ (-K)^{-1/2} \sinh[(-K)^{1/2}\chi], & (K < 0) \end{cases} \quad (4.10)$$

and  $\bar{\Gamma}(\chi) = 0$ , and hence the image remains undistorted with only an isotropic focusing. The differential equation for the first order quantities  $\delta\Lambda = \Lambda - \bar{\Lambda}$  and  $\delta\Gamma = \Gamma - \bar{\Gamma}$  are

$$\ddot{\delta\Lambda} = -(K\delta\Lambda + \bar{D}\delta\mathcal{R}), \quad \ddot{\delta\Gamma} = -(K\delta\Gamma + \bar{D}\delta\mathcal{F}), \quad (4.11)$$

which are integrated with the initial conditions  $0 = \delta\Lambda = \delta\Gamma = \dot{\delta\Lambda} = \dot{\delta\Gamma}$  as

$$\delta\Lambda(\chi) = - \int_0^\chi d\chi' \delta\mathcal{R}(\chi') \bar{D}(\chi') \bar{D}(\chi - \chi'), \quad (4.12)$$

$$\delta\Gamma(\chi) = - \int_0^\chi d\chi' \delta\mathcal{F}(\chi') \bar{D}(\chi') \bar{D}(\chi - \chi'). \quad (4.13)$$

Note that  $\delta\Lambda$  is real, so that there is no rotation in the image to this order. Let us define

$$\kappa = -\delta\Lambda/\bar{D}, \quad \gamma = \delta\Gamma/\bar{D}. \quad (4.14)$$

The amplification of the brightness of images relative to that in a homogenous universe is given by  $(\bar{D}/D)^2 = 1 + 2\kappa$  to first order, so  $\kappa$  (convergence) measures the fluctuation in the image brightness due to the lensing by the density inhomogeneity. Similarly  $\gamma$  (shear) is a dimensionless measure of the image distortion due to the lensing.

The sources  $\delta\mathcal{R}$  and  $\delta\mathcal{F}$  of the image distortion are stochastic variables which average to zero:  $\langle\delta\mathcal{R}\rangle = \langle\delta\mathcal{F}\rangle = 0$ . To evaluate the statistical properties of this distortion, it is convenient to Fourier-transform the density field at time  $\eta$  as  $\tilde{\delta}(\mathbf{k}, \eta) = \int d^3\mathbf{x} \delta(\mathbf{x}, \eta) \exp(-i\mathbf{k}\cdot\mathbf{x})$  (valid for  $k^2 \gg |K|$ ) and define the power spectrum  $P(k, \eta)$  as  $\langle\tilde{\delta}(\mathbf{k}, \eta) \tilde{\delta}(\mathbf{k}', \eta)\rangle = (2\pi)^3 P(k, \eta) \delta_D(\mathbf{k} - \mathbf{k}')$ . Then from Eq. (4.8) the two point correlation of  $\delta\mathcal{R}$  at two locations  $\mathbf{x}$  and  $\mathbf{x}'$  is

$$\langle\delta\mathcal{R}(\mathbf{x}) \delta\mathcal{R}(\mathbf{x}')\rangle = \frac{9}{4} \Omega_0^2 \int \frac{d^3\mathbf{k}}{(2\pi)^3} \frac{P(k, \eta)}{a^2(\eta)} \exp[i\mathbf{k}\cdot(\mathbf{x} - \mathbf{x}')]. \quad (4.15)$$

Below we calculate the two point correlations of convergence  $\langle \kappa_A \kappa_B \rangle$  and shear  $\langle \gamma_A \gamma_B^* \rangle$  between images A and B at the same redshifts separated by a small angle vector  $\boldsymbol{\theta}$  on the sky. Since the integrals in Eqs. (4.12) and (4.13) can be performed along the unperturbed path to first order,  $\mathbf{k} \cdot (\mathbf{x} - \mathbf{x}')$  in the exponent is written as  $\mathbf{k}_\perp \cdot \boldsymbol{\theta} \bar{D}(\chi) + k_\parallel (\chi - \chi')$  where  $\mathbf{k}_\perp$  (or  $k_\parallel$ ) is the wavenumber perpendicular (or parallel) to the line of sight. When  $\theta \ll 1$  we can approximate  $k_\parallel \ll k_\perp$  and obtain

$$\langle \delta \mathcal{R}(\mathbf{x}) \delta \mathcal{R}(\mathbf{x}') \rangle = \frac{9\pi}{4} \Omega_0^2 \delta_D(\chi - \chi') \int_0^\infty \frac{dk}{k} \frac{\Delta^2(k, \eta)}{k a^2(\eta)} J_0[k\theta \bar{D}(\chi)], \quad (4.16)$$

where  $\Delta^2(k, \eta) = k^3 P(k, \eta)/(2\pi^2)$ . A similar calculation shows that  $\langle \delta \mathcal{F}(\mathbf{x}) \delta \mathcal{F}^*(\mathbf{x}') \rangle = \langle \delta \mathcal{R}(\mathbf{x}) \delta \mathcal{R}(\mathbf{x}') \rangle$  and  $\langle \delta \mathcal{R}(\mathbf{x}) \delta \mathcal{F}(\mathbf{x}') \rangle = 0$ . From Eqs. (4.12), (4.13) and (4.16) there results \*)

$$\begin{aligned} C(\theta) &= \langle \kappa_A \kappa_B \rangle = \langle \gamma_A \gamma_B^* \rangle \\ &= \frac{9\pi}{4} \Omega_0^2 \int_0^\chi d\chi' \frac{\bar{D}^2(\chi') \bar{D}^2(\chi - \chi')}{\bar{D}^2(\chi)} \\ &\quad \times \int_0^\infty \frac{dk}{k} \frac{\Delta^2(k, \chi')}{k a^2(\chi')} J_0[k\theta \bar{D}(\chi')], \end{aligned} \quad (4.17)$$

where  $a(\chi')$  is given as Eq. (4.9).

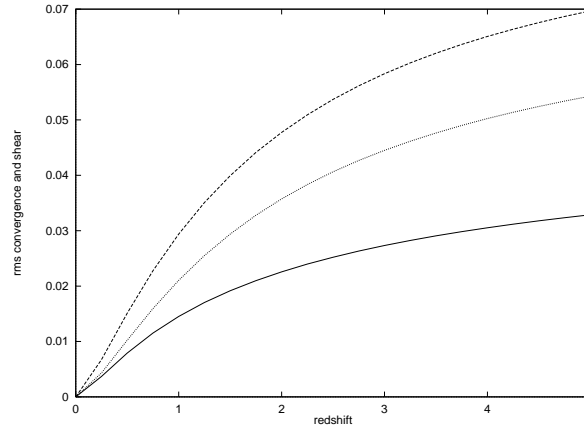


Fig. 12. Rms convergence and shear  $C^{1/2}(0) = \langle \kappa^2 \rangle^{1/2} = \langle |\gamma|^2 \rangle^{1/2}$  as a function of the source redshift. The solid, dashed and dotted curves correspond to  $(\Omega_0, \lambda_0, \sigma_8) = (1, 0, 0.5)$ ,  $(0.3, 0, 1)$ ,  $(0.3, 0.7, 1)$ .

In Fig. 12 the root-mean-square convergence and shear  $C^{1/2}(0) = \langle \kappa^2 \rangle^{1/2} = \langle |\gamma|^2 \rangle^{1/2}$  is plotted versus the source redshift, and in Fig. 13 the square root of the two point correlation  $C^{1/2}(\theta) = \langle \kappa_A \kappa_B \rangle^{1/2} = \langle \gamma_A \gamma_B^* \rangle^{1/2}$  of convergence and shear between images A and B at redshift  $z = 2$  is plotted versus the separation angle  $\theta$  on the sky. We use the non-linear power spectrum with the shape parameter  $\Omega_0 h = 0.25$ ,<sup>64)</sup> which reproduces well the nearby galaxy survey data. The solid,

\*) In conventional units, Eq. (4.17) should be divided by  $(c/H_0)^4$ .

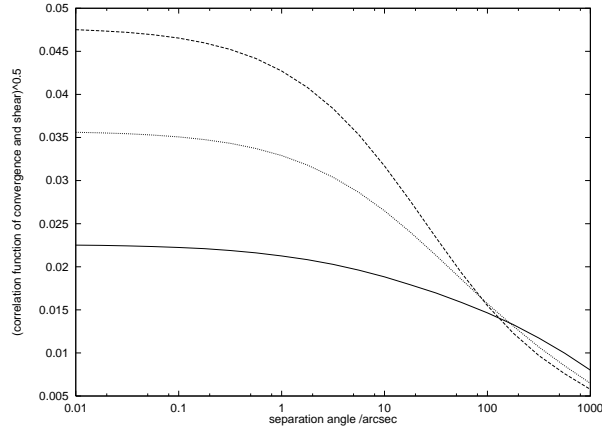


Fig. 13. Two point correlation  $C^{1/2}(\theta) = \langle \kappa_A \kappa_B \rangle^{1/2} = \langle \gamma_A \gamma_B^* \rangle^{1/2}$  of convergence and shear between images A and B at redshift  $z = 2$  as a function of the separation angle  $\theta$  in the sky. The solid, dashed and dotted curves correspond to  $(\Omega_0, \lambda_0, \sigma_8) = (1, 0, 0.5), (0.3, 0, 1), (0.3, 0.7, 1)$ .

dashed and dotted curves in the figures correspond respectively to the cosmological models with  $(\Omega_0, \lambda_0, \sigma_8) = (1, 0, 0.5), (0.3, 0, 1), (0.3, 0.7, 1)$  (standard, open and cosmological-constant models), where the normalizations  $\sigma_8$  of the power spectrum on the  $8\text{Mpc}/h$  scale are chosen such that the observed abundance of low-redshift clusters is consistent with the prediction of Press–Schechter theory.<sup>65)</sup> The figures represent the result for an infinitesimal source size because we do not smooth the density field; for a finite source the density field should be smoothed on the scale of the source size.

Since we are using a power spectrum well-constrained by the observational data at  $z \sim 0$ , the differences between the curves in the figures purely reflect the different behavior of backward light propagation into the past in these cosmological models. Intuitively, the rms amplification and shear should be larger in higher density universes, as explained by the overall factor  $\Omega_0^2$  in Eq. (4.17). However Fig. 12 shows that this effect is overwhelmed by the evolutionary effect of the density inhomogeneity: the growth of the density contrast in the standard (or open) model is fastest (or slowest) among the three models according to the gravitational instability picture.<sup>66)</sup> Since a fast growth implies that the inhomogeneity is rapidly erased as one goes to the past, the lensing effect in the standard (or open) model is smallest (or largest) in Fig. 12. Therefore the detection of cosmic shear should allow us to probe the growth of the large-scale density inhomogeneity, when combined with observational constraints for  $z \sim 0$ . On the other hand, Fig. 13 shows that in the open (or standard) model the decrease of correlation with increasing angle is fastest (or slowest). This is due to the cosmological geometry (Eqs.(4.9) and (4.10)): for fixed  $\theta$  and  $z$  the physical separation  $\theta \bar{D}$  in the open (or standard) model is largest (or smallest) among the three models. Thus the slope of the correlation function of cosmic shear,  $dC/d \ln \theta$ , should be a measure of the geometry of our universe.

### §5. Concluding remarks

In §2 it was shown that the multi-lens-plane method can treat many ray bundles and realistic galaxy lens models in very useful and practical ways to derive statistical behavior of strong and weak lensing owing to the simplicity of the calculations. The discussion in §3 shows that the recent progress in supercomputers has made it possible to use the direct integration methods for lensing analyses, and that non-galactic lens objects on galactic scales (if any) may have more important influences on the cosmological lensing (than galactic lenses) on small-angle scales ( $< 1$  min) depending on the lensing models. In §4 it was shown that perturbative methods based on the CDM power spectrum are very useful for analyses of weak lensing on large-angle scales ( $\gg 1$  min).

For the lensing correction to the luminosity of small objects such as super novae we must treat ray bundles with small separation angles ( $\leq 2$  arcsec) for which the deflection due to the small-scale matter distribution on galactic scales is important. From the analysis in §3 it is found that the correction can be larger by a factor of  $\sim 5$  than that due to the perturbative methods.<sup>67)</sup>

### Acknowledgements

K.T. would like to thank Y. Suto for helpful discussions about  $N$ -body simulations. His numerical computations were performed on the YITP computer system. P.W.P. is indebted to H. Martel for his help in preparing the manuscript, to T. Futamase for his valuable advice, and to the JSPS for a postdoctoral fellowship. Her computational works was performed on the University of Texas High Performance Computing Facility funded through R. Matzner.

### References

- [1] J. E. Gunn, *Astrophys. J.* **147** (1967), 61.
- [2] J. E. Gunn, *Astrophys. J.* **150** (1967), 737.
- [3] S. Weinberg, *Astrophys. J.* **208** (1976), L1.
- [4] R. D. Blandford and M. Jaroszyński, *Astrophys. J.* **246** (1981), 1.
- [5] P. Schneider, J. Ehlers and E. E. Falco, *Gravitational Lenses* (Springer-Verlag, Berlin, 1992).
- [6] R. D. Blandford and R. Narayan, *Astrophys. J.* **310** (1986), 568.
- [7] P. Schneider and A. Weiss, *Astrophys. J.* **327** (1988), 526.
- [8] P. Schneider and A. Weiss, *Astrophys. J.* **330** (1988), 1.
- [9] M. Jaroszyński, C. Park, B. Paczyński and J. R. Gott III, *Astrophys. J.* **365** (1990), 22.
- [10] M. Jaroszyński, *Mon. Not. R. Astron. Soc.* **249** (1991), 430.
- [11] M. Jaroszyński, *Mon. Not. R. Astron. Soc.* **255** (1992), 655.
- [12] B. Paczyński and J. Wambsganss, *Astrophys. J.* **337** (1989), 581.
- [13] M. H. Lee and B. Paczyński, *Astrophys. J.* **357** (1990), 32.
- [14] J. Wambsganss, R. Cen, J. P. Ostriker and E. L. Turner, *Science* **268** (1995), 274.
- [15] J. Wambsganss, R. Cen and J. P. Ostriker, *Astrophys. J.* **494** (1998), 29.
- [16] P. Premadi, H. Martel and R. Matzner, *Astrophys. J.* **493** (1998), 10.
- [17] R. K. Sachs, *Proc. R. Soc. London* **A264** (1961), 309.
- [18] R. Kantowski, *Astrophys. J.* **155** (1969), 89.
- [19] C. C. Dyer and R. C. Roeder, *Astrophys. J.* **189** (1974), 167.
- [20] R. Kantowski, *Astrophys. J.* **447** (1995), 35.

- [21] K. Watanabe and K. Tomita, *Astrophys. J.* **355** (1990), 1.
- [22] D. E. Holz and R. M. Wald, *Phys. Rev.* **D58** (1998), 063501.
- [23] C. C. Dyer and L. M. Oattes, *Astrophys. J.* **326** (1988), 50.
- [24] D. E. Holz, *Astrophys. J.* **506** (1998), L1.
- [25] K. Tomita and K. Watanabe, *Prog. Theor. Phys.* **82** (1989), 563.
- [26] K. Tomita and K. Watanabe, *Prog. Theor. Phys.* **83** (1990), 467.
- [27] A. Kashlinski, *Astrophys. J.* **331** (1988), L1.
- [28] K. Tomita, *Publ. Astron. Soc. Jpn.* **40** (1988), 751.
- [29] K. Tomita, *Phys. Rev.* **D40** (1989), 3821.
- [30] M. Sasaki, *Mon. Not. R. Astron. Soc.* **240** (1989), 415.
- [31] K. Tomita, *Prog. Theor. Phys.* **99** (1998), 97.
- [32] K. Tomita, *astro-ph/9806003*.
- [33] K. Tomita, *Prog. Theor. Phys.* **100** (1998), 79.
- [34] A. Babul and M. H. Lee, *Mon. Not. R. Astron. Soc.* **250** (1991), 407.
- [35] R. D. Blandford, A. B. Saust, T. G. Brainerd and J. V. Villumsen, *Astrophys. J.* **251** (1991), 600.
- [36] J. Villumsen, *Mon. Not. R. Astron. Soc.* **281** (1996), 369.
- [37] F. Bernardeau, L. Van Waerbeke and Y. Mellier, *Astron. Astrophys.* **322** (1997), 1.
- [38] T. T. Nakamura, *Publ. Astron. Soc. Jpn.* **49** (1997), 151.
- [39] V. E. Linder, *Mon. Not. R. Astron. Soc.* **243** (1990), 353., **243** (1990), 362.
- [40] E. Martinez-Gonzalez, J. L. Sanz and J. Silk, *Phys. Rev.* **D46** (1992), 4193.
- [41] E. Martinez-Gonzalez and J. L. Sanz, *Astrophys. J.* **484** (1997), 1.
- [42] L. Cayon, E. Martinez-Gonzalez and J. L. Sanz, *Astrophys. J.* **403** (1993), 471.
- [43] U. Seljak, *Astrophys. J.* **463** (1996), 1.
- [44] B. Jain and U. Seljak, *Astrophys. J.* **484** (1997), 560.
- [45] R. W. Hockney and J. W. Eastwood, *Computer Simulation using Particles* (New York, McGraw-Hill, 1981)
- [46] H. Martel, P. Premadi and R. Matzner, *Astrophys. J.* **497** (1998), 512.
- [47] G. Efstathiou, R. S. Ellis and B. A. Peterson, *Mon. Not. R. Astron. Soc.* **232** (1988), 431.
- [48] E. F. Bunn and M. White, *Astrophys. J.* **480** (1997), 6.
- [49] Y. Suto, *Prog. Theor. Phys.* **90** (1993), 1173.
- [50] E. Bertschinger, *astro-ph/9506070*.
- [51] S. Perlmutter et al., *Astrophys. J.* **483** (1997), 565.
- [52] A. G. Riess et al., *Astron. J.* **116** (1998), 1009.
- [53] B. Ford, Y. Miller, M. Dantel-Fort, H. Bonnet and J.-P. Kneib, *Astron. Astrophys.* **310** (1996), 705.
- [54] P. Schneider, L. van Waerkebe, Y. Miller, B. Jain, S. Seits and B. Ford, *Astron. Astrophys.* **333** (1998), 767.
- [55] C. W. Misner, K. S. Thorne and J. A. Wheeler, *Gravitation* (Freeman, San Francisco, 1973).
- [56] M. Sasaki, *Mon. Not. R. Astron. Soc.* **228** (1987), 653.
- [57] T. Futamase and M. Sasaki, *Phys. Rev.* **D40** (1989), 2502.
- [58] T. Watanabe and M. Sasaki, *Publ. Astron. Soc. Jpn.* **42** (1990), L33.
- [59] J. Miralda-Escudé, *Astrophys. J.* **380** (1991), 1.
- [60] N. Kaiser, *Astrophys. J.* **388** (1992), 272.
- [61] S. Seitz and P. Schneider, *Astron. Astrophys.* **287** (1994), 349.
- [62] R. Bar-Kana, *Astrophys. J.* **468** (1996), 17.
- [63] M. Sasaki, *Prog. Theor. Phys.* **90** (1993), 753.
- [64] J. A. Peacock and S. J. Dodds, *Mon. Not. R. Astron. Soc.* **267** (1994), 1020.
- [65] T. Kitayama and Y. Suto, *Astrophys. J.* **490** (1997), 557.
- [66] P. J. E. Peebles, *The Large-Scale Structure of the Universe* (Princeton University Press, Princeton, 1980).
- [67] J. A. Frieman, *Comments Astrophys.* **18** (1997), 323.